






Increased electron transfer kinetics and thermally treated graphite stability through improved tunneling paths

O. Charles Nwamba^{1,4,*} , Elena Echeverria² , Qiong Yu¹ , Krishnan S. Raja³ , David N. McIlroy² , Jean'ne M. Shreeve¹ , and D. Eric Aston^{3,*} 

¹Department of Chemistry, University of Idaho, 875 Perimeter Drive MS 2343, Moscow, ID 83844, USA

²Department of Physics, Oklahoma State University, 145 Physical Science Bldg., Stillwater, OK 74078, USA

³Department of Chemical and Materials Engineering, University of Idaho, 875 Perimeter Drive MS 1021, Moscow, ID 83844, USA

⁴Present address: Chemistry and Nanoscience Centre, National Renewable Energy Laboratory, 15013 Denver West Parkway, Golden, CO 80414, USA

Received: 13 April 2020

Accepted: 16 May 2020

Published online:
27 May 2020

© Springer Science+Business
Media, LLC, part of Springer
Nature 2020

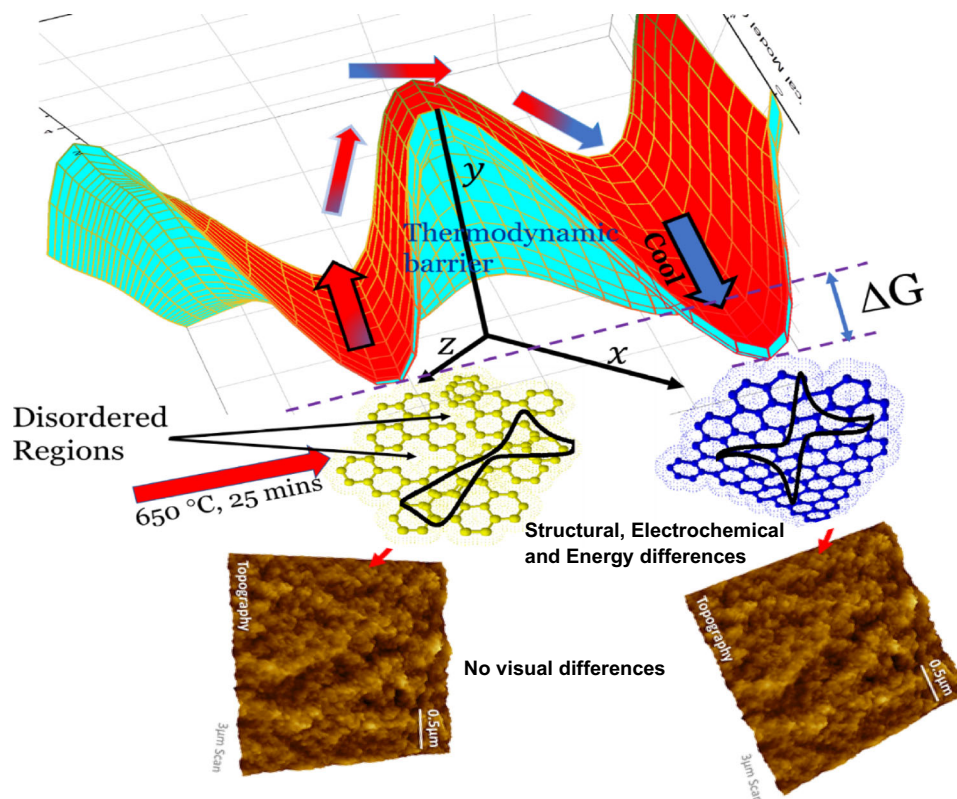
ABSTRACT

Aging of graphite-based materials results in slower heterogeneous electron transfer (HET) kinetics and limits their conducting and catalytic performance. A thermal treatment protocol reportedly maintained a high HET kinetics of graphite by at least nine weeks. The present report investigates the consequences of such HET increases on graphite stabilities. Raman 2D peak evolution, potential windows, EIS, optical AFM, chronoamperometry and potentiodynamic polarization studies were employed to investigate electrochemical, structural and corrosion stabilities and mechanisms of the pristine and thermally treated graphite as they relate to its HET kinetics. Structure-induced electronic changes are suggested to trigger improved tunneling paths through the interfaces from the bulk layer. This tunneling improves and sustains HET kinetics by orders of magnitude in the treated graphite. Except for the graphite fibers, thermal treatment increased HET kinetics without compromises to electrochemical, structural and corrosion stabilities. In most instances, these properties improved over the pristine graphite.

Address correspondence to E-mail: nwam5645@vandals.uidaho.edu; Charles.nwamba@NREL.gov; aston@uidaho.edu

GRAPHIC ABSTRACT

Thermal treatment transforms the pristine graphite into well-ordered lattices. AFM images show visual indifference between the pristine and treated graphite. However, their electronic structures and resultant electrochemistry are different. Despite minimal energy differences between both structures, a large thermodynamic barrier hinders the reversal of the treated to the pristine-like state.



Introduction

For over 60 years, active research in the carbon field has sought to know why and how carbon materials, especially graphite/graphitic materials—with inherently low electronic conductivity—experience degradation in electron transfer kinetics on air/solution exposure [1–7]. At most times, this decay in heterogeneous electron transfer (HET) kinetics is of the order of minutes to hours [8–13]. HET kinetics is fundamental in solid carbon electrode–electrolyte interactions, determining the performance of

materials in electrochemical applications [10, 14] and playing significant roles in molecular electronics, electrochemical energy storage/conversion, sensing and electro-oxidative reactions [9, 15–23]. Several techniques have been employed to restore the HET kinetics of carbonaceous materials after air- or solution-induced oxidation (viz., aging). Such procedures include mechanical polishing as commonly employed on glassy carbon electrodes, vacuum heat treatment or heat treatment under an inert gas atmosphere. Included, also, are combined treatments such as laser-based thermal treatment protocols,

electrochemical polarization such as pre-anodization and plasma activation protocols such as radio-frequency plasma, among many others [7, 24, 25]. Despite several remedial strategies employed to date, the issue of slower HET due to aging remains a major limitation on the use of carbon materials in many applications. Every activation protocol employed thus far has sustained HET kinetics by just a few hours at most [5–7, 24–31].

Recently, a thermal treatment protocol was reported to have tuned the electronics of eight different graphite samples [32]. This electronic tuning increased and sustained their HET kinetics for at least nine weeks while boosting the capacitance of the treated graphite felts. The thermally treated graphite@Prussian blue specimens, as shown by cyclic voltammograms in another study, were stable for up to 36 h in a neutral solution. That finding showed superior performance after thermal treatment in contrast to other reports on untreated graphitic materials@Prussian blue or their composites [33]. These results raise the question of the functional and structural stabilities of these treated materials. This is because there have been several reports of trade-off in stability/longevity in carbon materials, platinum and other electrode materials with good electronic conductivity. Such good electronic conductivity and fast HET usually result in materials/electrode degradation [34–38], such as increased corrosion rates [34, 39, 40]. The question therefore is: what is the trade-off, as regards material stability, for this kind of fast and sustained HET kinetics in the thermally treated graphite?

The present report also addresses the contributions of electrode texture/structure and morphology to the electrochemical properties of the treated graphite on which the rate of electron transfer at carbon electrodes depends [41]. For example, even within 2D materials, graphenes have more defects (in textural contexts such as surface wrinkles) than carbon nanotubes (CNTs) [42–44]. These defects ensure that graphenes, and similarly MoS₂, have more density of states (DOS) than CNTs [42–44] and therefore better electrochemical [10, 45, 46] and even mechanical properties [42–44]. The key questions formulated include the following: (a) Are surface defects (such as wrinkles, roughness) responsible for the fast and sustained HET kinetics of the treated graphite? 2D materials have ordered layer stacking, which is reportedly responsible for most of their electrochemical properties [47–49]. (b) Is the fast electron transfer kinetic of the treated graphite related to the

ordered stacking of their graphene sheets? (c) If ordered layer stacking in graphite occurs on thermal treatment, to what extent would this stacking influence the use of these treated graphite samples for applications as graphite intercalation compounds (GICs)? (d) If the treated materials could be used as GICs (GICs are graphite with highly tunable inter-layer spaces, which can accommodate a variety of ions and molecules [50]), what is the importance of texture and morphology such as smooth, clean interfaces (or roughness) [51, 52] and mechanical flexibility (or rigidity) [50] to the staging phenomenon in GICs? This is because graphite morphology is suggested to be tightly connected with the intercalation process [53]. (e) How does thermal treatment affect the potential windows of the various graphite samples employed in this study in terms of their hydrogen and oxygen evolution potentials?

To address the questions above, six types of graphite samples with different textures and morphologies were investigated, such as: (i) pyrolytic graphite from Panasonic (PG(Panasonic)): thin, flexible with rough or uneven surface, (ii) PG(K&J): thick, rigid, hard with coarse/corrugated surface, (iii) artificial graphite: thin, flexible with smooth surface, (iv) graphite (Equalseal): thick, rigid and brittle, soft and with smooth surface, (v) graphite rod: solid, packed particles, rough and coarse surface with circular exposed areas and (vi) GFA3 (graphite fiber with approximately 3 mm fiber thickness): soft, flexible and fibrous, with finely bundled fibers (see Figure S1 for images of these materials).

Experimental

Methods

Chemicals and materials

All materials, chemicals and reagents were used as received from the suppliers: flexible pyrolytic graphite (PG) sheets (Panasonic Electronic Components: 115 × 180 × 0.025 mm³ thick, gray, part number EYG-S121803) (Digi-Key Electronics, Thief River Falls, MN, USA); plain (no insert) flexible graphite (Equalseal, [Warren, OH]) sheets (8.25" × 9.5" × 1/16"), Acros Organics (Bridgewater, NJ, USA); artificial graphite sheets (T68; 50 mm × 20 mm × 25 μm) (t-Global Technology Co. Ltd, Taiwan); pyrolytic graphite blocks, PG1 (32 ± 2 mm × 16 ± 2 mm × 0.75 ± 0.5 mm thick, K &

J Magnetics [Plumsteadville, PA, USA]); graphite rods (40767-KD: graphite rod, 6.15 mm (0.242 in) dia. \times 152 mm (6 in) long, 99.9995% (metals basis, Alfa Aesar [Haverhill, MA, USA]); graphite blocks (99.99%, $40 \times 40 \times 3$ mm³ thick) Maibang Carbon (Henan, Mainland China); Ag/AgCl/3 M NaCl (aq) reference electrodes (0.209 V vs. SHE) and reference electrode cells (Bioanalytical Systems Inc (BASi), West Lafayette, IN, USA)); battery felt SIGRACELL® GFA3 ($297 \times 210 \times 3$ mm³ thick) and soft felt SIGRATHERM GFA5 ($297 \times 210 \times 5$ mm³, SGL Carbon Company GmbH [Meitingen, Germany]); Advanced abrasives (Sand-Blaster, 3 M [St. Paul, MN, USA]); Teflon tape (Dupont, [Elk Grove Village, IL]); low resistance copper foil tape with conductive adhesive ($0.25'' \times 1296'' \times 0.0011''$ thick, Kraftex® [Woodchester, Stroud, England]); premium microscope slides (plain, Fisher Scientific, USA); loctite clear silicone waterproof sealant (Westlake, OH, USA); and GE silicone 2 + (General Electric [Huntsville, NC, USA]).

Chemicals: potassium hexacyanoferrate (III) ($\text{Fe}(\text{CN})_6^{3/4-}$; ACS reagent, $\geq 99.0\%$) and potassium chloride crystal (SigmaUltra; $> 99.0\%$, Sigma Chemical Co., [St. Louis, MO, USA]); sodium sulfate crystals (Na_2SO_4 ; ACS reagent, 99.0%) (Alfa Aesar, Tewksbury, MA). All aqueous stock solutions were prepared with MilliQ® ($18 \text{ M}\Omega \text{ cm}^{-1}$) water.

Sample preparation for thermal treatment

Flexible graphite sheets, PG sheets, battery felt SIGRACELL® GFA3 and graphite rods were cut into pieces of ca. 4–5 cm long. One end of each cut graphite rod piece was polished with a 100-grit sandblaster followed by a finishing polish with a 320-grit sandblaster. The PG blocks were exfoliated using Scotch® tape [54], to expose fresh and pristine surfaces prior to thermal treatment and/or the start of control experiments using these pristine surfaces.

Thermal treatment

The thermal treatment protocol for graphite samples in air for 25 min at 650°C is reported [32]. After thermal treatment, the samples were cooled slowly to room temperature inside the furnace. The tube furnace was a high-temperature Lindberg/Blue M-type model furnace [Thermo Scientific (Asheville, NC, USA)].

Spectroscopy measurements

Raman spectroscopy

Raman scattering spectra were collected using a WITec™ alpha 300 R instrument (GmbH, Germany) with a 100-mW, frequency-doubled Nd:YAG ($\lambda = 532.5$ nm) laser focused with a $20 \times$ Nikon objective (NA = 0.4, WD = 3.9 mm) to a spot size of the order of $10 \mu\text{m}$, as described elsewhere [32]. Manual attenuation of the laser power to approximately 5 mW (sample incidence) reduces fluorescence and thermally induced artifacts prior to spectral acquisition to achieve sufficient signal-to-noise quality for graphite band comparisons at roughly similar conditions.

Ten single-spectrum “spot” scans over 0.50 s integration time via a UHT-300 spectrometer (grating = 600 grooves/mm, entrance aperture = $50 \mu\text{m}$) with an Andor™ DU970N-BV CCD array detector (1600×200 pixels) produce an average spectrum for comparison from three distinct and random sample locations. Spectral averages from near the surface, subsurface and deep-layer levels were acquired with optical images saved for each sample location through the same objective. Raman spectra were collected from visually defect-free sample locations, far from obvious edge exposures, for samples with visible defects or edge exposures, as judged from their acquired and now saved optical images.

Optical/atomic force microscopy (AFM)

The combined light microscopy with AFM single-platform instrumentation technique for high-resolution image acquisition of the pristine and treated pyrolytic graphite (K&J) was carried out as previously reported [55].

Ultraviolet photoelectron spectroscopy (UPS)

Binding energies were determined from ultraviolet photoelectron spectroscopy (UPS) in an ultrahigh vacuum (UHV) with a base pressure $< 10^{-10}$ Torr: dual anode XR 04–548 X-ray lamp (Physical Electronics); Al-sK α source operated at 400 W; X-ray incident angle of 54.7° and normal emission; Omicron EA 125 hemispherical energy analyzer, 0.02 eV

resolution, using both He I (21.2 eV) and He II (40.8 eV) excitation lines.

Thermal stability determinations

Thermogravimetric analysis (TGA)

Thermogravimetric analysis (TGA) of pristine and treated samples came from the TGA Q50 V20.13 Build 39 (TA Instruments; New Castle, DE, USA). Sample incineration in a platinum pan with a standard furnace ramped the temperature from baseline to 1000 °C at 10 °C/min under nitrogen flowing at 60 mL/min. Samples initially between 1 and 5 mg were weighed again after cooling to room temperature.

Electrode preparation for electrochemical measurements

Electrodes were made by fixing one side of the graphite to a glass slide with silicon grease. Low-resistance copper foil tape was attached to one end of the graphite and run through the entire length of the glass slide. A small length was extended further for attachment to the potentiostat. The working electrode area (0.3 cm² for graphite rods, ca. 1.0 cm² for GFA3 and ca. 0.50 cm² for other graphite) was exposed to electrolytes by insulating other graphite areas with sealants.

Electrochemical measurements

Cyclic voltammetry

Cyclic voltammetry (CV) studies of the various graphite samples, as working electrodes, were performed with a VersaStat 3 potentiostat/galvanostat (Princeton Applied Research). Graphite blocks (99.99%, 40 × 40 × 3 mm³ thick) served as the counter electrodes, while Ag/AgCl (3 M NaCl) were the reference electrodes. A 1 mM [Fe(CN)₆]^{3−/4−} (1 M KCl) solution served as the electrolyte and redox probe for the determination of the HET kinetics of the graphite investigated. The CVs of the graphite in 1 mM [Fe(CN)₆]^{3−/4−} (1 M KCl) were performed in triplicates for each graphite. Several CV runs were done for each in this redox probe to ensure voltammogram stability and reproducibility. CVs and other electrochemical measurements were performed within hours to several days after thermal treatment of the graphite. Pristine GFA3

electrodes were made hydrophilic by wetting in acetone and then rinsing with copious amounts of MilliQ® water. For the present report, ferricyanide/ferrocyanide (Fe(CN)₆^{3−/4−}) served as the redox couple to probe the HET kinetics of the graphite electrodes for three main reasons. First, Fe(CN)₆^{3−/4−} is stable, soluble and undergoes a rapid outer-sphere mechanism involving one-electron exchange [5]. Second, Fe(CN)₆^{3−/4−} is sensitive to surface oxides on carbon electrodes [11, 56]. Third, with Fe(CN)₆^{3−/4−}, there is minimum bonding interaction between the carbon electrode material and the cations in solution [41]. Then, the resultant electrochemistry would not be attributed to charge-transfer complexes from surface bonding interactions [57]. The implication is that the redox probe is meant to reflect and respond to sluggishness in electron transfer kinetics from adsorbed oxides on the electrode surfaces [11, 56]. These oxides have been implicated in aging [58, 59]. Thus, a widening ΔE_p from Fe(CN)₆^{3−/4−} is an indication that the electrode is aging. The converse would suggest that the aging phenomenon is not necessarily due to surface contaminants like the oxides and methyl (−CH₂) groups previously reported [32].

Potential window determination

Cyclic voltammetry to determine the cathodic and anodic potential limits for the onset of hydrogen and oxygen evolution, respectively, at defined current densities was carried out in a 1 M H₂SO₄ solution—purged with nitrogen prior to and during cathodic CV runs.

Chronoamperometry study

Controlled potential coulometry experiments, for each graphite pair of pristine and thermally treated samples, were conducted at 1.6 V in 0.10 M Na₂SO₄ for 24 h using a Gamry Interface 1000 Potentiostat/Galvanostat/ZRA (Gamry Instruments, [Hartsville, PA, USA]). The electrolysis experiments were performed in a 1 L reaction vessel. The counter electrode was a 15 × 9.5 × 0.5-cm³-thick, high-surface-area GFA5 felt.

Potentiodynamic polarization studies

Potentiodynamic studies were performed in a 1L reaction vessel using 0.10 M Na₂SO₄ as the electrolyte. The counter electrode (15 × 9.5 × 0.5 cm³)

was the high-surface-area GFA5 felt. Prior to start of the potential scans, an open circuit potential (OCP) was run, while continuously being purged with nitrogen gas and stirring, for at least 90 min and the values stored. Potential scans ranged between -0.3 and 1.8 V (vs Ag/AgCl reference electrode) at 1 mV/s, with the graphite materials serving as the working electrodes. Continuous purging with nitrogen gas while stirring simultaneously was maintained throughout the OCP runs and potentiodynamic scans.

Electrochemical impedance spectroscopy (EIS) study

Potentiostatic EIS measurements at room temperature with a Gamry Reference 600 Potentiostat/Galvanostat/ZRA- (Gamry Instruments, [Hartsville, PA, USA]) used a $15 \times 9.5 \times 0.5$ cm³ piece of GFA5 felt as the counter electrode. EIS was carried out at open circuit potentials (OCP) vs Ag/AgCl reference electrode by superimposing an AC signal of 10 mV (rms) on the OCP and scanning the frequency from 10 kHz to 10 mHz and collecting ten data points per decade of frequency range.

Data processing

Microsoft Excel 2016® version and Origin version 2018b® facilitated all data processing. The Origin graph plotting component produced all graphs, and the curve-fitting for Raman 2D bands used the non-linear least-square fitter based on the Levenberg–Marquardt algorithm.

Results and discussion

To answer the concerns raised in Introduction and the questions in (a) through (e) above, Raman spectroscopy was employed to probe the graphene layer stacking in the graphite using the 2D band evolutions and excursions. This investigation would lead to a better understanding of how ordered (or disordered) stacking of the graphite layers influences the observed electrochemistry of the treated compared to the pristine graphite. Typically, a Raman 2D peak changes from a one-peak to a four-peak band for single to bilayer graphene transition [60–62]. As the graphene layer increases to more than five sheets, the 2D spectrum becomes similar to that of bulk graphite

[61, 62]. A typical Raman 2D graphite spectrum has two peaks [62–66], consistent with that of multilayer graphene (greater than five layers) [61, 62], and indicative of 3D ordering [65, 66]. The Raman 2D band curve-fittings (viz. vibrational mode reconstructions) of the pristine and treated graphites and their corresponding optical images are shown in Figs. 1 and S2. The pristine PG (Panasonic) curve-fitting shows three likely vibrational modes (Figure 1a), while that of the treated sample shows seven fitted modes (Fig. 1b).

These results suggest that the pristine samples have some level of layer ordering, while the treated sample is well ordered. Besides, their optical images are similar (Fig. 1c, d). The pristine and treated graphite, respectively, of Equalseal (Fig. 1e, f), PG (K&J) (Fig. 1j, f), graphite rod (Figure S2a, b) and GFA3 (Figure S2 e, f) curve-fittings show two peaks each. These fits are characteristic of graphite (3D material) and indicate anisotropy in their layer orderings. The curve-fittings of the pristine and treated artificial graphite have multiple fits, consistent with isotropic graphene stacking traits previously thought unique to only 2D materials [67]. The curve-fittings of the pristine samples of PG (Panasonic) (Fig. 1a), and artificial graphite (Fig. 1m) are suggestive of an ABCA (rhombohedral) stacking order. The curve-fittings of the treated samples of the PG (Panasonic) (Fig. 1b) and artificial graphite (Fig. 1n) are suggestive of an ABAB (Bernal) stacking order [68, 69]. The ABAB stacking is thermodynamically more stable to those of the ABCA-type stacking [70]. These configuration differences would influence their electrochemical responses. The graphite images in Figs. 1 and S2 show no observable differences in morphology. Although optical imagery is not conclusive on its own at this stage, it will suggest that the differences in Raman spectra are not from morphological differences.

Since Raman spectroscopy correlates well with X-ray diffraction (XRD) data in terms of crystallinity determination, via the determination of the in-plane crystallite spacing, L_a from Raman data [66, 71, 72], we had previously used Raman data to calculate the in-plane crystallite spacing along the a-axis (L_a) [32]. In that report, we surmised that except for the graphite rods and natural graphite (the reason is that the overall electronics of these graphite species is predominant over their defect ratio, I_D/I_G), the decrease in L_a between planes corresponds to an increase in

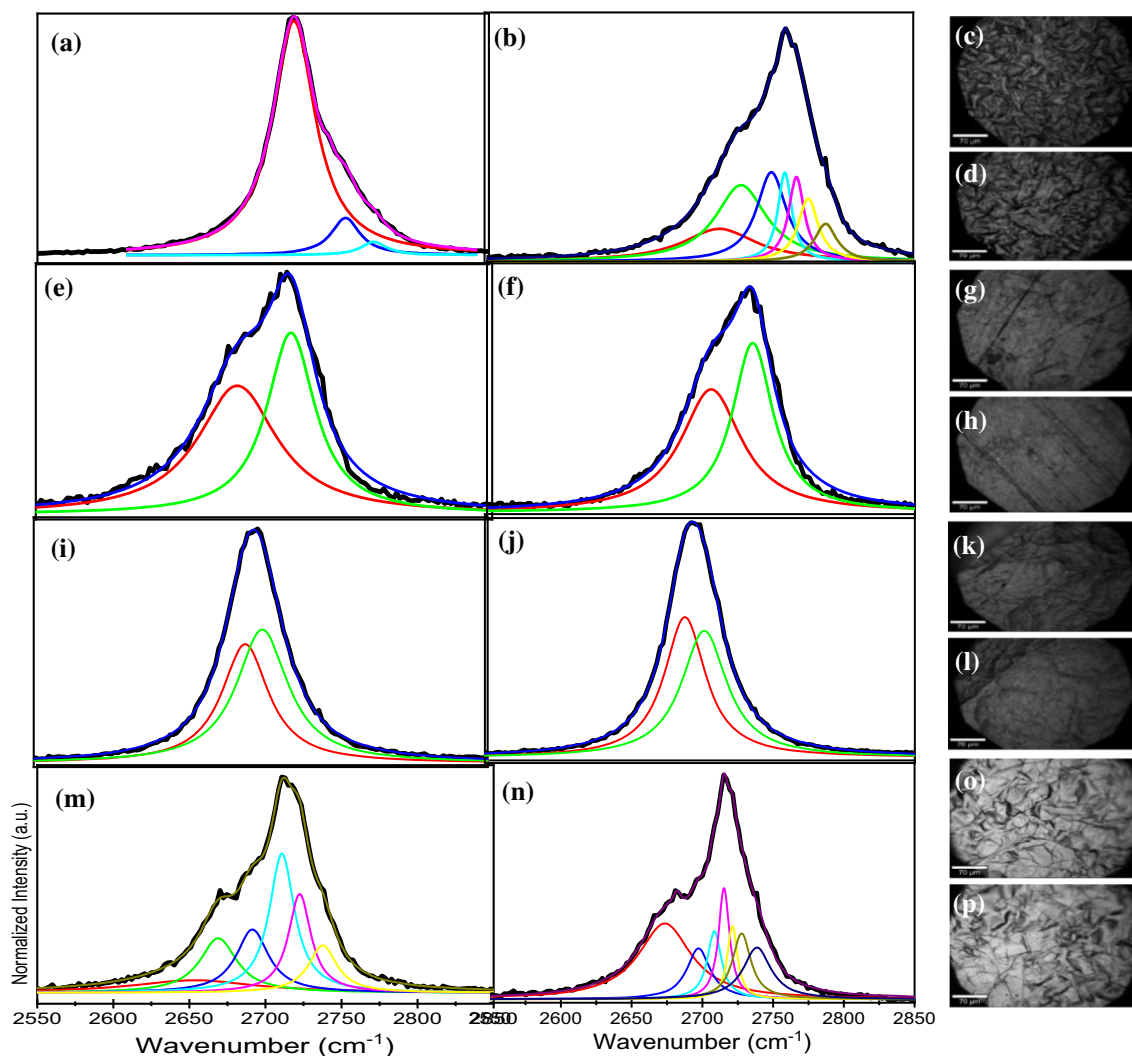


Figure 1 Deconvolved Raman 2D band of pristine and treated (a, b) PG (Panasonic), (e, f) graphite (Equalseal), (i, j) PG (K&J), and (m, n) artificial graphite. Optical images, respectively, of pristine and treated (c, d) PG (Panasonic), (g, h) graphite (Equalseal), (k,

i) PG (K&J) and (o, p) artificial graphite. The scale bars are 70 μm for each optical image. The full Raman spectra of all graphite in this study are in Figure S3.

the crystallite sizes. The trend indicated a transition from a diffusive (in the pristine) to a lamellar structure on thermal treatment [66, 73]. This transition results in well-ordered hexagonal or honeycomb-like structures with good electrical conductivities [74].

TGA data could be used to relate structures to bonding-induced stability of materials. The TGA results of graphite (Equalseal), PG (K&J) and PG(Panasonic) are shown in Fig. 2a–c, while those of GFA3, artificial graphite and graphite rod are shown in Figure S4a–c. Figure 2a inset shows that the pristine sample has a steeper mass change (ΔP) at about 200–400 $^{\circ}\text{C}$ compared to the treated sample (ΔT). These data indicate different pathways to their

thermal degradation and by inference, different structures. The same is true for the other graphite samples studied. Even though the decomposition temperatures for each sample pair are the same or nearly the same (ca. 770–800 $^{\circ}\text{C}$), the pristine samples experienced a more rapid incineration beyond their decomposition temperatures. Graphite rod is the exception: The treated sample has a steeper (faster) decomposition profile compared to its pristine (Figure S4c). The graphite rod rigidity may be responsible for this trend. The thermal stability of the treated relative to the pristine samples may arise from less disruption of the more crystalline nature of the treated materials [32, 75–77].

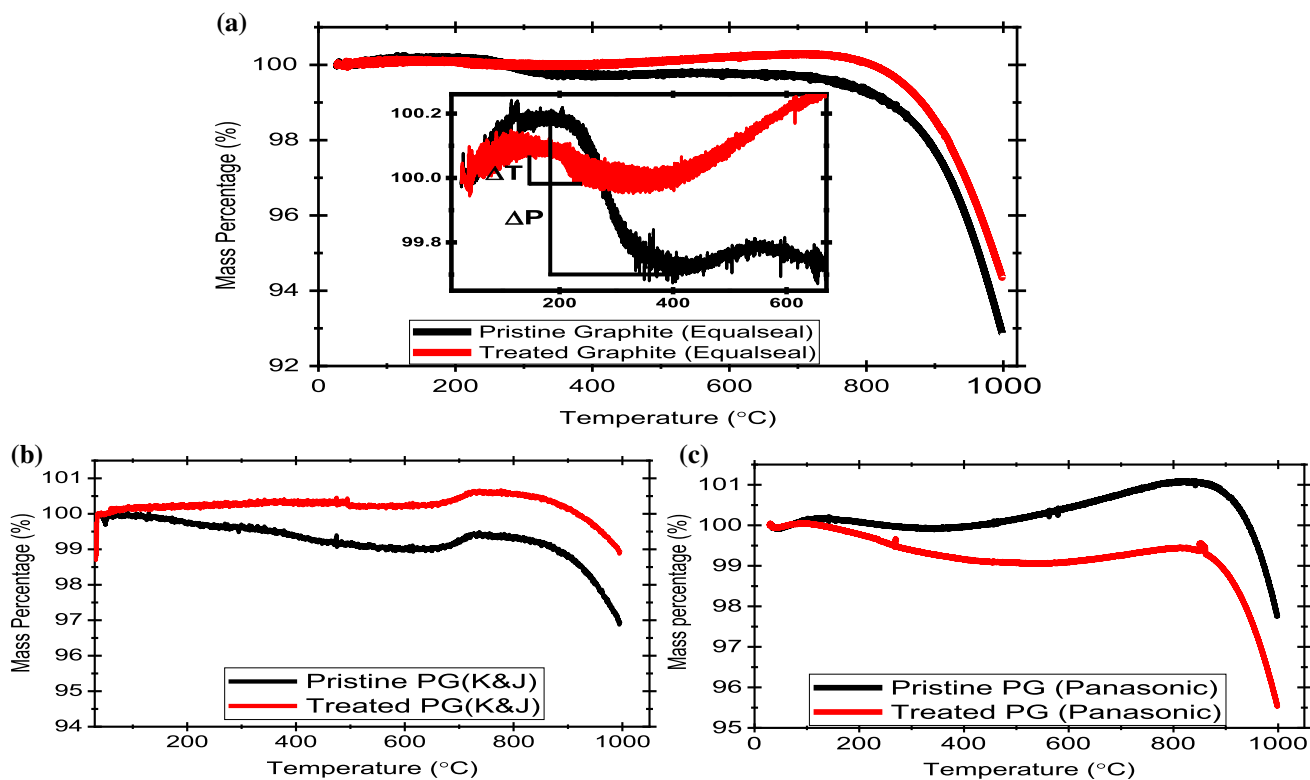


Figure 2 The thermogravimetric analysis (TGA) figures of pristine and treated samples of **a** Graphite (Equalseal). Inset zoom of 0–650 °C. **b** PG (K&J) and **c** PG (Panasonic).

The topographies of both PG (K&J) sets were probed further by light microscopy-coupled AFM [55]. The aim of these measurements was to check for possible surface modification from thermal treatment. The AFM scans of the pristine and treated PG (Fig. 3a, b, respectively, and Figure S5) from several locations show that the treated PG surface is more uneven compared to the pristine. The treated PG has craters of 0.30–0.35 μm in depth, while those of the pristine are 0.10–0.15 μm beneath the surface. Both graphite samples had similar grain sizes ca. 50–100 nm.

To investigate their interfacial reactivities in different electrolytes, the HOMO-level electronic spectra of the graphite were examined via ultraviolet photoelectron spectroscopy (UPS). The valence band maximum (VBM) energy relative to the Fermi energy ($E_{\text{F}} - E_{\text{VBM}}$ where $E_{\text{F}} = 0$ eV)—an energy position of the onset of the valence band state [78, 79]—and an indication of the potential for interfacial chemical reactions [80] of the treated and pristine samples were similar (Table 1). Trends seen in Fig. 4 appeared for all other graphite samples in this study (Figure S6). These results suggest that even though there

were structural differences and significant electronic band changes between both graphite sets [32], there were little-to-no structural influences on their potential interfacial reactions.

Same graphite species such as PG (K&J), GFA3, graphite rod and artificial graphite used in ref [32] (these graphite samples were used to check for consistency and reproducibility for this present paper in regard to the studies on thermally treated graphite) as well as some new graphite species [PG (Panasonic) and graphite (Equalseal)] were employed to assay for the electron transfer kinetics of the graphite employed in this study for the purpose of understanding the importance and consequences of the fast electron transfer kinetics on the stability of the thermally treated graphite. The cyclic voltammograms (CVs) in 1 mM $\text{Fe}(\text{CN})_6^{3-/4-}$ and 1 M H_2SO_4 for HET rates (k^0) and potential window values, respectively, are shown in Fig. 5. The k^0 values were determined using the Nicholson method [81]. The k^0 and potential window values (anodic and cathodic limits at 200 $\mu\text{A cm}^{-2}$ onset for oxygen and hydrogen evolution, respectively) are presented in Table 1.

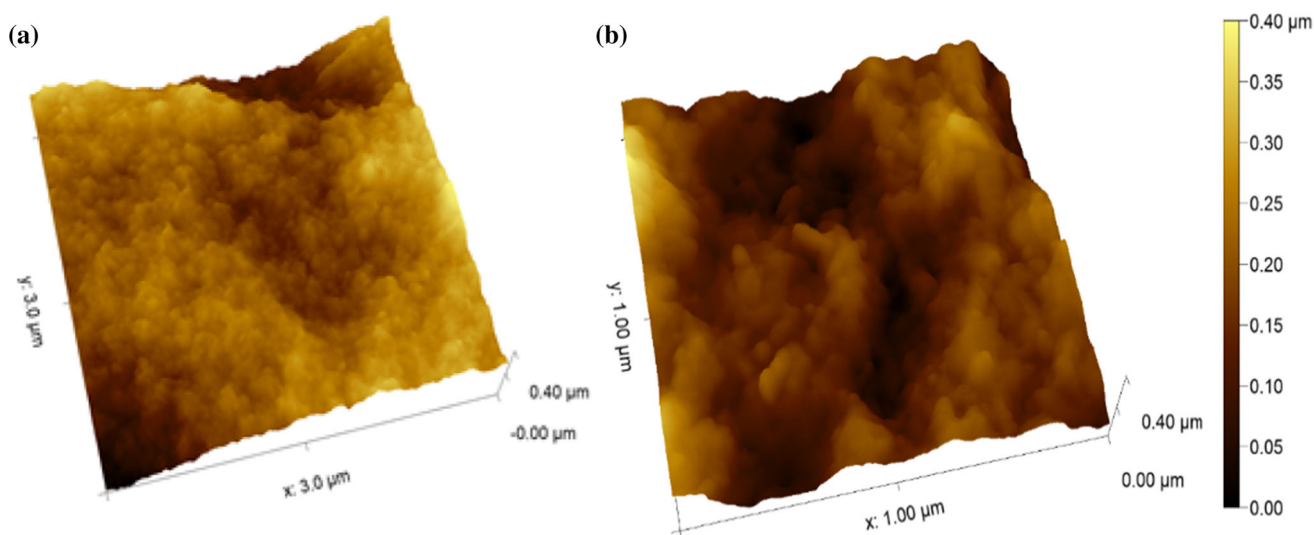


Figure 3 The AFM 3D topography of **a** pristine (3- μm scan) and **b** treated (1- μm scan) PG (K&J).

The HET kinetics in the current report—except for the GFA3—is very similar to those of ref.[32], suggesting reproducibility of k^0 even for the same graphite types bought at different times. New in this report (Table 1) is the importance of thermal treatment to the potential windows, corrosion properties and valence band maxima (VBM). The potential window values of the treated pyrolytic graphite (PG) and artificial graphite decreased by about 0.2 V with a twofold increase in k^0 , compared to the pristine samples (Fig. 5a–d, respectively). These potential window decreases were mainly from the cathodic and anodic limits of the PG and artificial graphite, respectively (Table 1).

The treated graphite (Equalseal) had nearly the same k^0 with a slight potential window increase of ca. 0.60 V over the pristine (Fig. 5bi). Also, the pristine sample anodic region reveals both a decreased potential and a large onset current density to oxygen evolution unlike the treated sample (Fig. 5bi). This result shows the susceptibility of the pristine sample to oxygen evolving reactions. The treated graphite rod showed k^0 increase of roughly an order of magnitude and potential window increase of ca. 0.30 V. With GFA3 as an exception, the increase in the treated graphite k^0 is independent of the textures and/or morphology of the graphite (Table 1). As for the treated GFA3, we ascribe the slight decrease in k^0 reported here to inhomogeneities from fiber preparation. This is because the treated GFA3 k^0 value was higher than its pristine counterpart in an earlier report [32], and slightly less in a later report [33].

These findings imply that electrons tunnel efficiently through the distances separating the thermally treated electrode surfaces from the redox probe irrespective of oxides on the treated graphite surfaces [25]. In contrast, the pristine graphite surface oxides lead to electrostatic repulsion from the redox probe, thereby resulting in larger electron tunneling distance—between the electrode and the $\text{Fe}(\text{CN})_6^{3-/4-}$ —and more sluggish kinetics [46, 82]. The treated PG (Panasonic) CVs in 1 M H_2SO_4 exhibited up to stage 1 ion intercalation unlike the pristine with only a stage “4 + 5” and a mild “1 + 2” (every stage set is numbered and designated with broken vertical lines in Fig. 5a (ii)). The intercalation inserts HSO_4^- (intercalant) into the graphene layers across the graphite basal planes to form a graphite- HSO_4^- complex [5, 53, 83]. The number of graphite layers between the intercalate layers is known as the “stage” number. Staging is the most important characteristic ordering property of GIC graphene sheets [5, 53, 83]. Also, staging reflects the degree of graphitization and crystalline perfection of graphite [5, 83]. It is suggested that thermal treatment-mediated conversion of the ABC (staggered)-type layering to the ABA (parallel) type is responsible for these differences in intercalation stages.

Thus, the PG (Panasonic) thermal treatment resulted in (a) increased material graphitization and crystalline perfection, (b) proper graphene stacking (from Raman data), (c) increased stages of intercalation and (d) increased HET kinetics as earlier reported [32, 33]. The pristine and treated graphite

Table 1 ΔE_p (mV) and accompanying rate constants, a cathodic and anodic limits of the potential windows @ 200 $\mu\text{A}/\text{cm}^2$ onset limit for hydrogen and oxygen evolution, respectively; corrosion currents (i_{corr}), potentials (E_{corr}) and valence band maxima (VBM) of the treated and pristine graphites

Electrode	Type	ΔE_p (mV)	a k^0 (cm s^{-1})	@ 200 $\mu\text{A}/\text{cm}^2$		Pot Window (V)	i_{corr} (A cm^{-2})	E_{corr} (mV)	VBM(eV)
				Cathode (V)	Anode (V)				
PG (K&J)	C	300 ± 28	3.74 ± 0.52 × 10 ⁻⁴	-1.05 ± 0.16	1.84 ± 0.11	2.89 ± 0.05	1.65 ± 0.25 × 10 ⁻⁹	32.45 ± 16.3	-3.99 ± 0.15
	T	68 ± 1	1.96 ± 0.24 × 10 ⁻²	-0.90 ± 0.01	1.80 ± 0.01	2.70 ± 0.003	4.51 ± 0.20 × 10 ⁻⁹	3.20 ± 24.3	-4.05 ± 0.05
PG (Panasonic)	C	345 ± 46	3.07 ± 0.58 × 10 ⁻⁴	-1.19 ± 0.04	1.81 ± 0.02	3.00 ± 0.02	1.09 ± 0.12 × 10 ⁻⁹	-136.40 ± 7.8	-4.20 ± 0.10
	T	66 ± 2	2.61 × 10 ⁻² ± (*)	-1.03 ± 0.01	1.75 ± 0.02	2.78 ± 0.01	6.78 ± 4.22 × 10 ⁻¹⁰	-113.45 ± 55.7	-4.08 ± 0.004
Graphite (Equalseal)	C	80 ± 5	8.69 ± 2.5 × 10 ⁻³	-0.55 ± 0.07	0.80 ± 0.05	1.35 ± 0.02	2.47 ± 0.50 × 10 ⁻⁸	-88.40 ± 2.3	-2.61 ± 0.70
	T	82 ± 6	7.60 ± 2.6 × 10 ⁻³	-0.83 ± 0.02	1.13 ± 0.04	1.96 ± 0.02	4.04 ± 2.23 × 10 ⁻⁹	-78.20 ± 5.5	-2.95 ± 0.65
GFA3	C	213 ± 25	6.47 ± 1.4 × 10 ⁻⁴	-0.59 ± 0.09	1.15 ± 0.06	1.74 ± 0.03	5.38 ± 6.71 × 10 ⁻⁷	-17.3 ± 30.1	-3.78 ± 0.28
	T	303 ± 29	3.68 ± 0.52 × 10 ⁻⁴	-0.77 ± 0.13	0.99 ± 0.06	1.76 ± 0.06	4.12 ± 2.96 × 10 ⁻⁶	-186 ± 89	-3.61 ± 0.69
Graphite Rod	C	61 ± 1	0.13 ± 0.04	-0.52 ± 0.05	0.82 ± 0.18	1.34 ± 0.12	5.31 ± 3.00 × 10 ⁻⁸	-71.03 ± 25.2	-3.29 ± 0.58
	T	40 ± 1	1.021 ± 0.04	-0.56 ± 0.08	0.83 ± 0.03	1.39 ± 0.05	4.17 ± 2.10 × 10 ⁻⁸	-100.5 ± 0.7	-3.63 ± 0.13
Artificial Graphite	C	564 ± 22	1.64 ± 0.08 × 10 ⁻⁴	-0.83 ± 0.01	1.97 ± 0.04	2.80 ± 0.03	—	—	-3.91 ± 0.08
	T	69 ± 2	1.79 ± 0.41 × 10 ⁻²	-0.84 ± 0.02	1.76 ± 0.01	2.60 ± 0.004	—	—	-3.98 ± 0.01

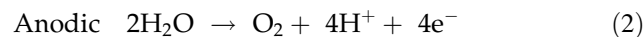
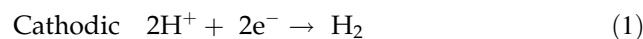
a k^0 [cm^2/s] in 1 mM Fe [(CN)₆]^{3-/4-} and at $v = 0.05$ V/s. $n = 3$.

C Control; T Treated.

(Equalseal) did not intercalate in 1 M H₂SO₄ (Fig. 5b(i)). No differences in intercalation occurred between the pristine and treated PG(K&J). However, the treated samples exhibited higher current density. The treated artificial graphite exhibited up to stage 1 ion intercalation (every stage set is designated with broken vertical lines in Fig. 5d(i)). The pristine artificial graphite had one stage (a “4 + 5”) intercalation (Fig. 5d(i)). With stage “1 + 2” intercalation, the treated PGs have properly stacked graphene sheets and exhibited both higher graphitization and crystalline perfection [5, 83]. Thus, Raman spectroscopy explains the increased staging of the treated PG during intercalation and corroborates the proper stacking order in the treated PG, gleaned from the increased intercalation staging in H₂SO₄ (Fig. 5d(i)).

In the treated PG (K&J), electronic tuning (higher graphitization and crystalline perfection) [32, 33] without ordered stacking made no difference to the intercalation stages. The graphite rods and GFA3 results were the same for their pristine and treated samples (Fig. 5e and f, respectively). The treated GFA3 displayed increased cathodic and anodic windows. These results suggest that in the absence of intercalation, thermal treatment increased the potential windows.

The CVs in 1 M H₂SO₄ (Fig. 5b(i)) also suggest that thermal treatment increased the overpotentials for hydrogen and oxygen evolution reactions (HER and OER) of treated graphite (Equalseal) due to loss of active sites for these reactions:



These two reactions are site specific for adsorption of water (H₂O) and H⁺ species. Surface defects are potential sites for adsorption of these species. Here, such sites are graphite edges (defects), carbon vacancies (point defects) and stacking defects [84]. The treated graphite has low edge defects (I_D/I_G from Raman data, see Figure S3b), and mainly ordered stacking (see discussion on Raman spectra). Therefore, the treated graphite has inherently low defect concentration and therefore shows high overpotentials for HER and OER [84]. Graphite (Equalseal) and graphite rod samples showed low anodic potential windows @ 200 $\mu\text{A}/\text{cm}^2$ (Table 1). These potentials being lower than the equilibrium potential for OER

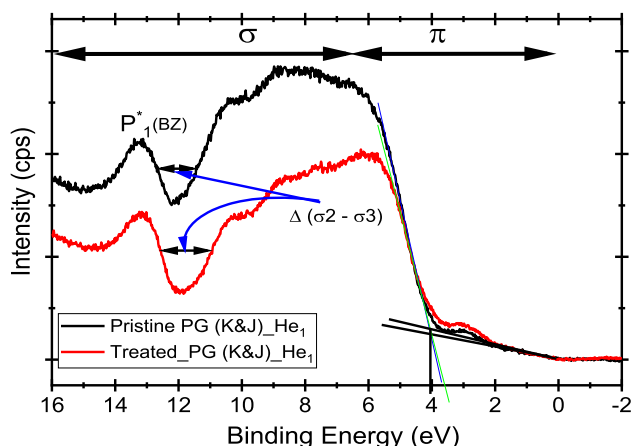
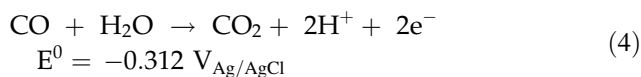
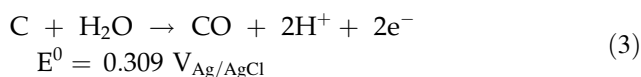


Figure 4 The electronic band structure of the pristine and treated PG(K&J) and the extrapolation method for Φ . P^*_1 is the vibrational density of states at the Brillouin zone (BZ).

(1.02 $V_{Ag/AgCl}$ in pH 0 solution) suggest anodic oxidation of the graphitic material by



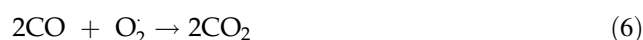
Thermal treatment improved the resistance to degradation of the Equalseal graphite as the anodic potential increased to 1.13 V from 0.8 $V_{Ag/AgCl}$.

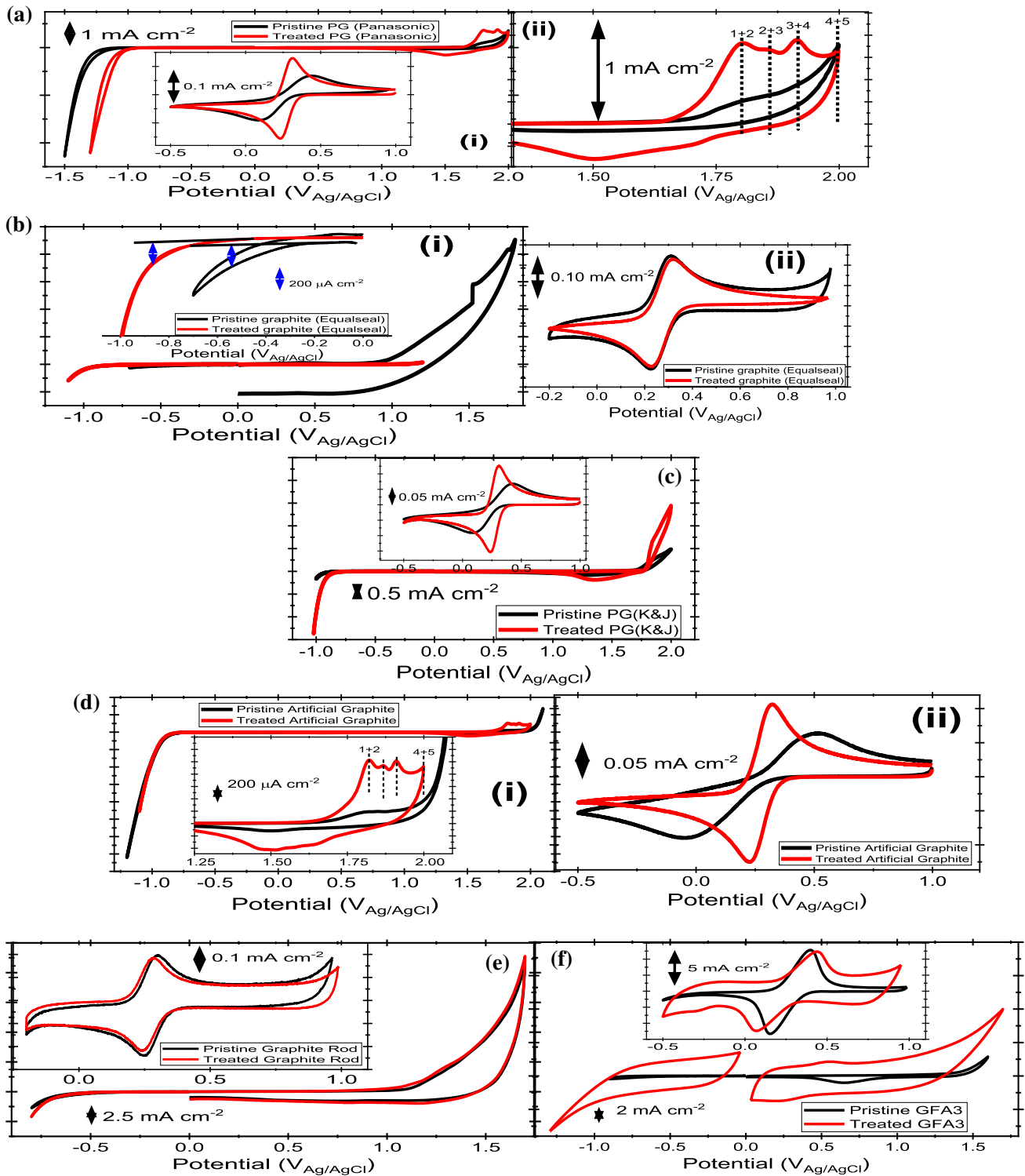
Thus, in answer to question (a), the fast HET kinetics of the thermally treated graphite is independent of surface textures (such as wrinkles or smoothness) or even morphology of the graphite. To question (b), which asked whether the fast electron transfer kinetics of the treated graphite are related to the ordered stacking of their graphene sheets, the answer is no! Ordered layer stacking is not responsible for the fast HET kinetics of the treated graphite. For question (c), which asked whether ordered stacking is important for GIC formation, the answer is yes! For “1 + 2” staging numbers, properly stacked graphenic sheets in the graphite are required even though that is not all that is required. Higher levels of graphitization and crystallinity are equally important for increased staging in GICs. For question (d), texture, such as smoothness or unevenness, is not a prerequisite for the graphite used as GICs in this study. PG (Panasonic) is thin, flexible with rough or uneven surfaces, while artificial graphite is thin, flexible with smooth surface. So, there were not any

differences between a smooth and an uneven surface for thin flexible sheets. Also, the rigid graphite (Equalseal, PG (K&J) and rods) showed no intercalation, implicating mechanical flexibility as important for GIC formation wherein rigidity hinders material expansion. Thus, for a graphitic material to have properties desirable for GICs, (i) ordered layer stacking, (ii) higher levels of graphitization and crystalline perfection and (iii) mechanical flexibility are a requirement. For question (e), the potential window decrease occurred where intercalation staging and or current densities are high (such as the two treated pyrolytic graphite types used in this report and treated artificial graphite). Otherwise, heat treatment resulted in potential window increase for the remainder of the graphite. It is also suggested that “activated” edges from thermal treatment might have lowered the cathodic limit (higher HER activity) of the thermally treated PG (Panasonic) [84].

To ascertain whether thermal treatment compromised the equilibrium corrosion properties of the treated graphite (structural stability issues) compared to their pristine samples, bulk electrolysis of the graphite was carried out at 1.6 V and in 0.10 M Na_2SO_4 solution. The results of these studies (Fig. 6 and Figure S7) show no compromise in stability of the treated graphite when used as anodes, despite the magnitude increases in k^0 for some of the samples.

For example, the treated PG current density was about the same as its pristine (Fig. 3a), even with two orders of magnitude difference in k^0 . The pristine Equalseal graphite had about a 1 mA/cm² higher current density relative to its treated sample (Fig. 6b) even with similar k^0 values (Table 1). The pristine PG was about 20 $\mu A/cm^2$ lower to the treated PG (Fig. 6c). Also, the pristine and treated graphite rods and GFA3 current densities (Figure S7a and S7b, respectively) were of the same order. Thus, the treated materials were not more vulnerable to possible degradation reactions than their pristine versions such as water hydrolysis to protons (intercalation of surface adsorbed H^+ within the graphene layers and crumbling of the layers) and oxygen, O_2 (which can degrade the carbon matrix via CO_2 evolution as shown in Eqs. 5 and 6).





◀ **Figure 5** Potential windows in 1 M H₂SO₄ of pristine and treated **a** PG (Panasonic) and **b** graphite (Equalseal). **a** Inset (i) cyclic voltammograms (CVs) for HET determination in 1 mM Fe(CN)₆^{3-/4-} (1 M KCl). (ii) Magnification of the anodic region (1.35–2.0 V) of different intercalation stages. **b** Inset (i) magnification of cathodic region of Equalseal to highlight decreased cathodic limit of pristine to treated material and to explain extrapolation method for the onset current at 200 μA/cm² for hydrogen evolution; (ii) CV for HET kinetics determination for pristine and treated graphite. **c** Pristine and treated PG(K&J) in H₂SO₄; inset CVs. **d** (i) Pristine and treated artificial graphite; inset of anodic arm to highlight increased intercalation of treated material at 200 μA/cm² on-set current for oxygen evolution. (ii) The CV of pristine and treated artificial graphite. **e** The potential window CVs of pristine and treated graphite rod. Insets are their CVs in Fe(CN)₆^{3-/4-}. **f** The potential window CVs of pristine and treated GFA3; inset CVs in Fe(CN)₆^{3-/4-}. CVs for both potential window and HET determination were run at $v = 0.05$ V/s.

It was shown that both graphite groups have essentially the same surface functional groups on air exposure [32]. Even though optical imagery has limited resolution to discriminate between both graphite sets, it is suggested that the treated graphite stability is not essentially due to their surfaces. Rather, it is suggested that increased graphitization accompanied by increased crystallinity on thermal treatment is responsible for the stability of the treated materials.

To quantify corrosion kinetics and deduce mechanisms, the corrosion current densities (i_{corr}) and potentials (E_{corr}) were extrapolated from their potentiodynamic scans using Tafel methods. The PG (K&J), graphite (Equalseal) and PG (Panasonic) results are shown in Fig. 7a–c, while graphite rod and GFA3 are shown in Figure S8a and S8b, respectively. Irrespective of the magnitude differences in k^0 between the pristine and treated samples, their i_{corr} and E_{corr} values were about the same (Table 1). The treated graphite (Equalseal) shows an i_{corr} value about an order of magnitude lower than that of untreated samples. On the other hand, the treated GFA3 showed about an order of magnitude higher i_{corr} than its pristine sample counterparts. The decrease in corrosion kinetics of the treated Equalseal graphite is suggested to be from thermal treatment induced decrease in the active site densities on their surfaces [77, 84] and from higher degree of crystallinity [77, 85].

The higher i_{corr} of the treated GFA3 than that of pristine samples could have been from fiber edge

exposure (Figure S3f), which are prone to oxidation [77]. The potentiodynamic scans suggest similar corrosion mechanisms for both graphite sets in 0.10 M Na₂SO₄. These results can be explained by noting that thermal treatment increases graphitization by causing increased crystallinity of graphitic materials [32, 76, 77]. Graphitization does not change the fundamental oxidation mechanism but slows down the carbon oxidation reaction [86]. This explains the similarity in corrosion mechanisms of the pristine and treated graphite samples even though the treated samples have, in some cases, two orders of magnitude higher k^0 relative to their equivalent pristine samples. These results imply that the treatment causes ballistic and sustained electron transport without changes in corrosion kinetics relative to the pristine samples. Since potentiodynamic polarization and bulk electrolysis are surface techniques, the actual factor(s) that reflected on the surface chemistry of the treated materials may be dictated mainly by structure-induced electronic features. Very similar VBM values would account for similar interfacial properties such as corrosion kinetics, thermodynamics and even mechanisms of the pristine and treated graphite. Since there were no apparent differences in the corrosion parameters of both graphite groups, the treated graphite step edges are not primarily responsible for the facile HET kinetics of the treated graphite basal planes [11, 34, 77, 86].

Electrochemical impedance spectroscopy (EIS) is important for understanding the interfacial properties of electrode materials [87] and how this interfacial property can affect the ability of material surfaces to transfer and exchange charges with a solution [88, 89]. The aim of this experiment was to understand the graphite–solution interfaces: how the treated graphite could have such fast HET kinetics in Fe(CN)₆^{3-/4-} and show similar corrosion kinetics and mechanisms in 0.10 M Na₂SO₄. To better understand the graphite–aqueous interfacial reactions, EIS of PG (K&J) in Na₂SO₄ was carried out as a model for the other graphite. The OCP of the treated graphite was 0.153 ± 0.05 V, while that of the pristine was 0.101 ± 0.04 V. The results, from the pristine and treated PG Nyquist plots (Fig. 8) and their corresponding equivalent circuit model (Fig. 8 inset), suggest a constant phase element (CPE) character for both electrode materials. Their corresponding Bode plots are presented in Figure S9. The parameters

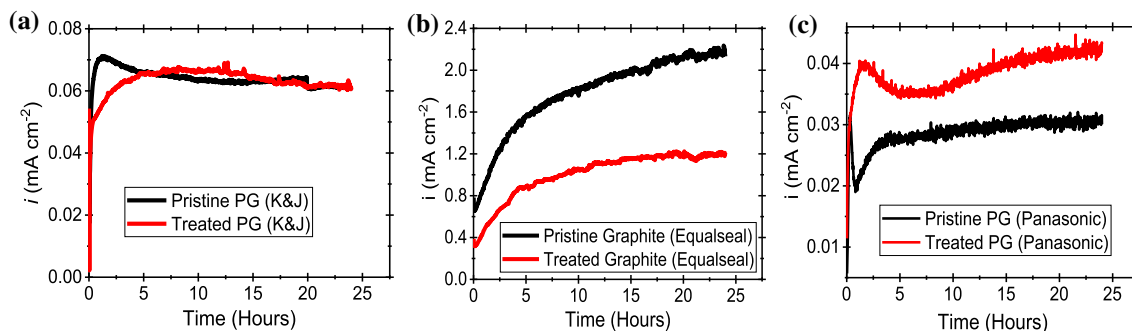


Figure 6 Bulk electrolysis in 0.10 M Na_2SO_4 for 24 h at 1.6 V for pristine and treated **a** PG (K&J), **b** graphite (Equalseal) and **c** PG (Panasonic).

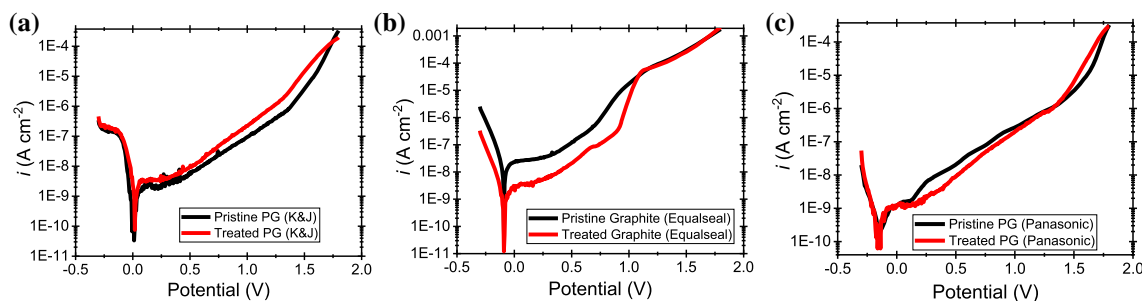


Figure 7 Potentiodynamic studies in 0.10 M Na_2SO_4 for 24 h at 1.6 V for pristine and treated **a** PG (K&J), **b** graphite (Equalseal) and **c** PG (Panasonic).

describing the interfacial properties from the equivalent circuit model are shown in Table 2.

The charge transfer parameter or interfacial resistance (R_{ct}) of the treated PG is six orders of magnitude greater than the pristine, while the treated PG capacitance parameter (Y_0) doubles over that of the pristine. The capacitance increase agrees with earlier reports for the treated graphite [32, 33]. The parameter α represents surface heterogeneity or continuously distributed time constants. The surface heterogeneity or the number of time constants increases when α decreases from unity. An ideal capacitor behavior is seen when $\alpha = 1$. More or less similar α value of the pristine and treated PG indicates that the surface roughness was not significantly affected by the treatment. Therefore, the difference in impedance could be attributed to the inherent changes in the electronic properties after thermal treatment and not to modification of the surface morphology. To better understand the significant increase in the R_{ct} values of the treated graphite, the EIS data were fitted with a two-time-constant equivalent electrical circuit as shown in Figure S9c. The EIS data of the treated graphite could be fitted with a

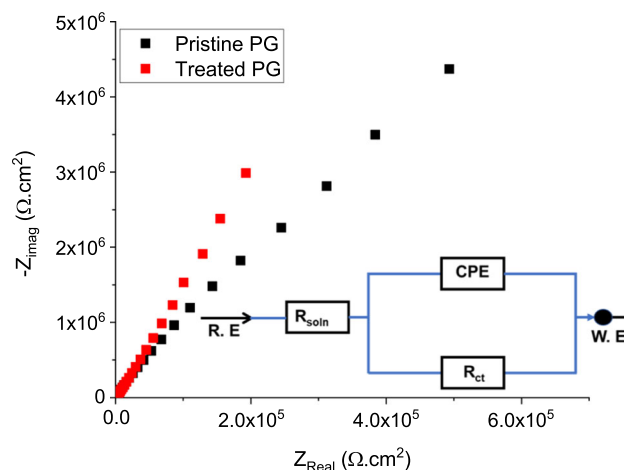


Figure 8 Nyquist plots of pristine and treated PG (K&J) in 0.10 M Na_2SO_4 . Inset equivalent circuit diagram.

much lower χ^2 value (i.e., goodness of fit) than that of pristine graphite using a two-time-constant circuit. This indicated that thermal treatment of the PG resulted in two steps of charge transfer, which could not be clearly discerned by the Nyquist or Bode plots.

High edge-defect concentration resulted in lower R_{ct} of the pristine PG. After thermal treatment, the

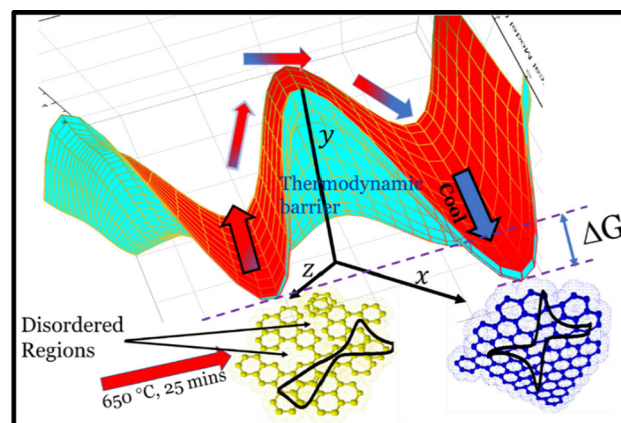
Table 2 Interfacial parameters derived from the CPE equivalent circuit model

	R_{ct} (Ω)	Y_0 ($S.s^{-2}$)	α	χ^2
Pristine PG	$4.64 \pm 4.2 \times 10^7$	$5.90 \pm 4.0 \times 10^{-6}$	0.951 ± 0.01	1.33×10^{-4}
Treated PG	$2.97 \pm 3.93 \times 10^{13}$	$1.13 \pm 0.93 \times 10^{-5}$	0.936 ± 0.02	2.70×10^{-3}

defects are predominantly annihilated but lattice ordering is improved, and specific surface area increased as seen from the AFM image (see discussion on AFM). Thus, the fast and sustained HET kinetics of the treated graphite is not a simple function of interfacial charge transfers between the treated electrode surfaces and their electrolytes. Also, the differences in R_{ct} are a testament to the differences in the structure and surface chemistry of both graphite sets [88, 89], even though they appear optically indistinguishable. Here, the high R_{ct} indicates the real corrosion resistance of the material. The thermally treated PG revealed higher corrosion resistance than that of pristine PG.

It appears that thermal treatment brought about conformational excursions over an energy barrier to a native state with correlated electronic structure (Scheme 1). Strong electronic correlations with weak σ electron–electron repulsion or strong π electron–electron interaction possess increased kinetic energy via quantum mechanical tunneling of the electrons in a crystal without the need for differences in interfacial reactivity (i.e., VBM). This increased π – to σ attribute increases conduction [90] and decreases corrosion [86, 91], as shown by our data (see Fig. 4). In addition, charge delocalization along the crystalline sites (Scheme 1) is no longer susceptible to surface bound oxides, methyl groups and electrostatic repulsion from $Fe(CN)_6^{3-/4-}$ [11, 32, 46], which also increases electron tunneling probability. Thus, enhanced electron tunneling (from the bulk to the surface)—the fast step—results in corrosion resistance of the thermally treated (structure-modified) graphite while facilitating and maintaining fast HET kinetics.

As a surface phenomenon, corrosion targets features that aid faster HET kinetics and that are more likely to contribute to and accelerate corrosion leading to material degradation [34]. However, the thermally treated graphite surfaces are conduits for electron transfer but are neither the originating sites for, nor the facilitators of, electron transfer. Thus, the structural and functional integrity of the treated



Scheme 1: A transverse depiction of the energy landscape for a generic pristine graphite with disordered regions and sluggish electron transfer kinetics represented by the quasi-reversible nature of the cyclic voltammogram (CV) in 1 mM $Fe(CN)_6^{3-/4-}$. On heating at 650 °C in air for 25 min, pristine graphite gains enough energy to transverse a huge thermodynamic barrier and cools to a polycrystalline state with well-ordered structure that facilitates facile electron transfer kinetics as seen by the reversible nature of its CV. Even though the barrier is large, the energy difference (ΔG) between both structures is small. This explains how polycrystalline structures formed on cooling do not revert to the pristine-like structure, thus ensuring sustained fast HET kinetics for many weeks.

graphite is maintained irrespective of accelerated HET kinetics.

Conclusion

In a general sense, thermal treatment resulted in fast HET kinetics without compromising electrochemical, thermal and corrosion stabilities of the treated graphites. In some instances, these properties even improved over the pristine graphite. Of the six graphite samples, only GFA3 had lower k^0 and higher i_{CORR} when treated, as ascribed to fiber inhomogeneity during preparation. Heat treatment abolished the level of anisotropy that is usually reported for graphite such that the thermally treated PG graphene layers are properly stacked. Thermal structural changes tuned the electronic structure to enhance π

over σ traits without changes in potentials for interfacial reactivity. This suggests that enhanced electron tunneling—via improved tunneling paths—is responsible for the ballistic HET kinetics and corrosion resistance improvements.

These findings suggest that the reported thermal treatment protocol would be suitable for graphite use in fuel cells as catalysts and catalyst support systems. Treated graphite samples with wide cathodic limits of over -1.0 V are candidates for electrocatalytic CO_2 reduction to liquid fuels. Thin, highly intercalating graphite would be appropriate as anode materials in batteries and other forms would serve effectively as supercapacitors for energy storage and as sensors. Other potential applications include catalysis, anodes for electro-oxidative reactions and applications where fast HET kinetics without material deterioration is a criterion.

Electronic supporting information

The Electronic Supporting Information is available free of charge on the Springer Publications Web site at DOI:

More information on the CVs, Raman spectroscopy and optical imaging, bulk electrolysis chronoamperograms, TGA results, Bode plots and circuit diagrams for EIS and AFM images.

Acknowledgements

OCN appreciates research funding from the College of Science and the College of Graduate Studies Deans' Offices and the Department of Chemical & Materials Engineering (UI). He also recognizes the Integrated Research and Innovation Center (IRIC) at the University of Idaho. Dr. Elisa M. Miller-Link of the Chemistry and Nanoscience Center, National Renewable Energy Laboratory, is warmly thanked for helpful discussions on photoelectron spectroscopy. The authors thank Angstrom Sciences, CA, for light microscopy/AFM image acquisitions.

Funding

This study was funded by the College of Science and the College of Graduate Studies Deans' Offices and

the Department of Chemical and Materials Engineering at the University of Idaho.

Compliance with ethical standards

Conflict of interest The authors declare that they have no conflict of interest.

Electronic supplementary material: The online version of this article (<https://doi.org/10.1007/s10853-020-04846-6>) contains supplementary material, which is available to authorized users.

References

- [1] Lord SS, Rogers LB (1954) Polarographic Studies with Gold, Graphite, and Platinum Electrodes. *Anal Chem* 26:284–295. <https://doi.org/10.1021/ac60086a009>
- [2] Gaylor VF, Elving PJ, Conrad AL (1953) Polarographic Oxidation of Phenolic Compounds. *Anal Chem* 25:1078–1082. <https://doi.org/10.1021/ac60079a022>
- [3] Adams RN (1958) Carbon Paste Electrodes. *Anal Chem* 30:1576. <https://doi.org/10.1021/ac60141a600>
- [4] Gaylor VF, Conrad AL, Landerl JH (1957) Use of a Wax-Impregnated Graphite Electrode in Polarography. *Anal Chem* 29:224–228. <https://doi.org/10.1021/ac60122a013>
- [5] Kinoshita K (1988) Carbon - Electrochemical and Physicochemical Properties. John Wiley & Sons Ltd, New Jersey
- [6] McCreery RL (1991) Carbon electrodes: structural effects on electron transfer kinetics. In: Bard AJ (ed) *Electroanalytical chemistry*, 17th edn. Marcel Dekker Inc., New York
- [7] Swain GM (2007) Solid electrode materials: pretreatment and activation. In: Zoski CG (ed) *Handbook of electrochemistry*, first. Elsevier B.V, Amsterdam, pp 111–153
- [8] Hu IF, Karweik DH, Kuwana T (1985) Activation and deactivation of glassy carbon electrodes. *J Electroanal Chem* 188:59–72. [https://doi.org/10.1016/0368-1874\(85\)85627-6](https://doi.org/10.1016/0368-1874(85)85627-6)
- [9] Velický M, Bradley DF, Cooper AJ et al (2014) Electron transfer kinetics on mono- and multilayer graphene. *ACS Nano* 8:10089–10100. <https://doi.org/10.1021/nm504298r>
- [10] Velický M, Bissett MA, Toth PS et al (2015) Electron transfer kinetics on natural crystals of MoS_2 and graphite. *Phys Chem Chem Phys* 17:17844–17853. <https://doi.org/10.1039/c5cp02490k>
- [11] Ji X, Banks CE, Crossley A, Compton RG (2006) Oxygenated edge plane sites slow the electron transfer of the ferro-/ferricyanide redox couple at graphite electrodes. *ChemPhysChem* 7:1337–1344. <https://doi.org/10.1002/cphc.200600098>

- [12] Patel AN, Collignon MG, OConnell MA et al (2012) A new view of electrochemistry at highly oriented pyrolytic graphite. *J Am Chem Soc* 134:20117–20130. <https://doi.org/10.1021/ja308615h>
- [13] Zhang G, Tan S, Patel AN, Unwin PR (2016) Electrochemistry of $\text{Fe}^{3+/2+}$ at highly oriented pyrolytic graphite (HOPG) electrodes: kinetics, identification of major electroactive sites and time effects on the response. *Phys Chem Chem Phys* 18:32387–32395. <https://doi.org/10.1039/C6CP06472H>
- [14] Laurila T, Sainio S, Caro M (2017) Hybrid carbon based nanomaterials for electrochemical detection of biomolecules. *Prog Mater Sci* 88:499–594. <https://doi.org/10.1016/j.pmatsci.2017.04.012>
- [15] Chandra S, Miller AD, Bendavid A et al (2014) Minimizing fouling at hydrogenated conical-tip carbon electrodes during dopamine detection in vivo. *Anal Chem* 86:2443–2450. <https://doi.org/10.1021/ac403283t>
- [16] Hu L, Peng X, Huo K et al (2016) Dominant factors governing the electron transfer kinetics and electrochemical biosensing properties of carbon nanofiber arrays. *ACS Appl Mater Interfaces* 8:28872–28879. <https://doi.org/10.1021/acsaami.6b10100>
- [17] Sofer Z, Jankovský O, Šimek P et al (2015) Insight into the mechanism of the thermal reduction of graphite oxide: deuterium-labeled graphite oxide is the key. *ACS Nano* 9:5478–5485. <https://doi.org/10.1021/acsnano.5b01463>
- [18] Mao X, Guo F, Yan EH et al (2016) Remarkably high heterogeneous electron transfer activity of carbon-nanotube-supported reduced graphene oxide. *Chem Mater* 28:7422–7432. <https://doi.org/10.1021/acs.chemmater.6b03024>
- [19] Parker JF, Kamm GE, McGovern AD et al (2017) Rewriting electron-transfer kinetics at pyrolytic carbon electrodes decorated with nanometric ruthenium oxide. *Langmuir* 33:9416–9425. <https://doi.org/10.1021/acs.langmuir.7b01107>
- [20] Taylor SM, Pătru A, Perego D et al (2018) Influence of carbon material properties on activity and stability of the negative electrode in vanadium redox flow batteries: a model electrode study. *ACS Appl Energy Mater* 1:1166–1174. <https://doi.org/10.1021/acsaem.7b00273>
- [21] Ferrari AC, Bonaccorso F, Fal'ko V et al (2015) Science and technology roadmap for graphene, related two-dimensional crystals, and hybrid systems. *Nanoscale* 7:4598–4810. <https://doi.org/10.1039/C4NR01600A>
- [22] Kong Y, Wang Z-L, Wang Y et al (2011) Degradation of methyl orange in artificial wastewater through electrochemical oxidation using exfoliated graphite electrode. *New Carbon Mater* 26:459–464. [https://doi.org/10.1016/S1872-5805\(11\)60092-9](https://doi.org/10.1016/S1872-5805(11)60092-9)
- [23] Maljaei A, Arami M, Mahmoodi NM (2009) Decolorization and aromatic ring degradation of colored textile wastewater using indirect electrochemical oxidation method. *Desalination* 249:1074–1078. <https://doi.org/10.1016/j.desal.2009.05.016>
- [24] Štulík K (1992) Activation of solid electrodes. *Electroanalysis* 4:829–834. <https://doi.org/10.1002/elan.1140040902>
- [25] McCreery RL (2008) Advanced carbon electrode materials for molecular electrochemistry. *Chem Rev* 108:2646–2687. <https://doi.org/10.1021/cr068076m>
- [26] Bowling RJ, Packard RT, McCreery RL (1989) Activation of highly ordered pyrolytic graphite for heterogeneous electron transfer: relationship between electrochemical performance and carbon microstructure. *J Am Chem Soc* 111:1217–1223. <https://doi.org/10.1021/ja00186a008>
- [27] Poon M, McCreery RL, Engstrom R (1988) Laser activation of carbon electrodes. Relationship between laser-induced surface effects and electron transfer activation. *Anal Chem* 60:1725–1730. <https://doi.org/10.1021/ac00168a018>
- [28] Bourke A, Miller MA, Lynch RP et al (2015) Electrode kinetics in all-vanadium flow batteries: effects of electrochemical treatment. *ECS Trans* 66:181–211. <https://doi.org/10.1149/06608.0181ecst>
- [29] Bourke A, Miller MA, Lynch RP et al (2015) Effect of cathodic and anodic treatments of carbon on the electrode kinetics of V IV /V V oxidation–reduction. *J Electrochem Soc* 162:A1547–A1555. <https://doi.org/10.1149/2.0671508jes>
- [30] Cumba LR, Foster CW, Brownson DAC et al (2016) Can the mechanical activation (polishing) of screen-printed electrodes enhance their electroanalytical response? *Analyst* 141:2791–2799. <https://doi.org/10.1039/c6an00167j>
- [31] Sawant TV, McKone JR (2019) Flow battery electroanalysis. 2. Influence of Surface Pretreatment on Fe(III/II) redox chemistry at carbon electrodes. *J Phys Chem C* 123:144–152. <https://doi.org/10.1021/acs.jpcc.8b09607>
- [32] Nwamba OC, Echeverria E, McIlroy DN et al (2019) Thermal modification of graphite for fast electron transport and increased capacitance. *ACS Appl Nano Mater* 2:228–240. <https://doi.org/10.1021/acsnm.8b01887>
- [33] Nwamba OC, Echeverria E, McIlroy DN et al (2019) Electrochemical stability and capacitance of in-situ synthesized Prussian blue on thermally-activated graphite. *SN Appl Sci* 1:731. <https://doi.org/10.1007/s42452-019-0713-z>
- [34] Frankel GS (2016) Fundamentals of corrosion kinetics. In: active protective coatings. In: Hughes A, Mol J, Zheludkevich MBR (eds) Springer series in materials science. Springer, Dordrecht, pp 17–32

- [35] Binninger T, Mohamed R, Patru A et al (2017) Stabilization of Pt nanoparticles due to electrochemical transistor switching of oxide support conductivity. *Chem Mater* 29:2831–2843. <https://doi.org/10.1021/acs.chemmater.6b04851>
- [36] Ghanim AH, Koonce JG, Hasa B et al (2018) Low-loading of Pt nanoparticles on 3D carbon foam support for highly active and stable hydrogen production. *Front Chem* 6:523. <https://doi.org/10.3389/fchem.2018.00523>
- [37] Sharma R, Rode Nielsen K, Brilner Lund P et al (2019) Sustainable platinum recycling through electrochemical dissolution of platinum nanoparticles from fuel cell electrodes. *ChemElectroChem* 6:4471–4482. <https://doi.org/10.1002/celec.201900846>
- [38] Robarts L, Santhanam KSV (2018) Interfacial Electron Transfer Involving Vanadium And Graphene Quantum Dots For Redox Flow Battery. *MRS Adv* 3:1221–1228. <https://doi.org/10.1557/adv.2018.153>
- [39] Henry PA, Raut AS, Ubnoske SM et al (2014) Enhanced electron transfer kinetics through hybrid graphene-carbon nanotube films. *Electrochem Commun* 48:103–106. <https://doi.org/10.1016/j.elecom.2014.08.024>
- [40] Wang X, Wang W, Lowry G et al (2018) Preparation of palladized carbon nanotubes encapsulated iron composites: highly efficient dechlorination for trichloroethylene and low corrosion of nanoiron. *R Soc Open Sci* 5:172242. <https://doi.org/10.1098/rsos.172242>
- [41] Nugent JM, Santhanam KSV, Rubio A, Ajayan PM (2001) Fast electron transfer kinetics on multiwalled carbon nanotube microbundle electrodes. *Nano Lett* 1:87–91. <https://doi.org/10.1021/nl005521z>
- [42] Rafiee MA, Rafiee J, Srivastava I et al (2010) Fracture and fatigue in graphene nanocomposites. *Small* 6:179–183. <https://doi.org/10.1002/sml.200901480>
- [43] Rafiee MA, Rafiee J, Wang Z et al (2009) Enhanced mechanical properties of nanocomposites at low graphene content. *ACS Nano* 3:3884–3890. <https://doi.org/10.1021/nn9010472>
- [44] Rafiee MA, Rafiee J, Yu ZZ, Koratkar N (2009) Buckling resistant graphene nanocomposites. *Appl Phys Lett* 95:223103. <https://doi.org/10.1063/1.3269637>
- [45] Zhong JH, Zhang J, Jin X et al (2014) Quantitative correlation between defect density and heterogeneous electron transfer rate of single layer graphene. *J Am Chem Soc* 136:16609–16617. <https://doi.org/10.1021/ja508965w>
- [46] Boopathi S, Narayanan TN, Senthil Kumar S (2014) Improved heterogeneous electron transfer kinetics of fluorinated graphene derivatives. *Nanoscale* 6:10140–10146. <https://doi.org/10.1039/c4nr02563f>
- [47] Xu J, Wang D, Lian R et al (2019) Structural Prediction and multilayer Li⁺ storage in two-dimensional VC₂ carbide studied by first-principles calculations. *J Mater Chem A* 7:8873–8881. <https://doi.org/10.1039/C9TA01476D>
- [48] Chia X, Pumera M (2018) Layered transition metal dichalcogenide electrochemistry: journey across the periodic table. *Chem Soc Rev* 47:5602–5613. <https://doi.org/10.1039/c7cs00846e>
- [49] Yu Y, Huang SY, Li Y et al (2014) Layer-dependent electrocatalysis of MoS₂ for hydrogen evolution. *Nano Lett* 14:553–558. <https://doi.org/10.1021/nl403620g>
- [50] Zhang M, Song X, Ou X, Tang Y (2019) Rechargeable batteries based on anion intercalation graphite cathodes. *Energy Storage Mater* 16:65–84. <https://doi.org/10.1016/j.ensm.2018.04.023>
- [51] Chen J, Fan X, Ji X et al (2018) Intercalation of Bi nanoparticles into graphite results in an ultra-fast and ultra-stable anode material for sodium-ion batteries. *Energy Environ Sci* 11:1218–1225. <https://doi.org/10.1039/c7ee03016a>
- [52] Zhang L, Peng S, Ding Y et al (2019) A graphite intercalation compound associated with liquid Na–K towards ultra-stable and high-capacity alkali metal anodes. *Energy Environ Sci* 12:1989–1998. <https://doi.org/10.1039/c9ee00437h>
- [53] Salvatore M, Carotenuto G, De Nicola S et al (2017) Synthesis and characterization of highly intercalated graphite bisulfate. *Nanoscale Res Lett* 12:167. <https://doi.org/10.1186/s11671-017-1930-2>
- [54] Geim AK, Novoselov KS (2007) The rise of graphene. *Nat Mater*. <https://doi.org/10.1038/nmat1849>
- [55] Erickson A, Ballinger T (2018) Ultra-thin AFM enables integration with light microscope. *Microsc Today* 26:28–33. <https://doi.org/10.1017/s1551929518001049>
- [56] Kuo T-C, McCreery RL (1999) Surface chemistry and electron-transfer kinetics of hydrogen-modified glassy carbon electrodes. *Anal Chem* 71:1553–1560. <https://doi.org/10.1021/ac9807666>
- [57] Otero R, Vázquez de Parga AL, Gallego JM (2017) Electronic, structural and chemical effects of charge-transfer at organic/inorganic interfaces. *Surf Sci Rep* 72:105–145. <https://doi.org/10.1016/j.surfrep.2017.03.001>
- [58] Li Z, Wang Y, Kozbial A et al (2013) Effect of airborne contaminants on the wettability of supported graphene and graphite. *Nat Mater* 12:925–931. <https://doi.org/10.1038/nmat3709>
- [59] Li Z, Kozbial A, Nioradze N et al (2016) Water protects graphitic surface from airborne hydrocarbon contamination. *ACS Nano* 10:349–359. <https://doi.org/10.1021/acs.nano.5b04843>

- [60] Pimenta MA, Dresselhaus G, Dresselhaus MS et al (2007) Studying disorder in graphite-based systems by Raman spectroscopy. *Phys Chem Chem Phys* 9:1276–1291
- [61] Ferrari AC, Meyer JC, Scardaci V et al (2006) Raman spectrum of graphene and graphene layers. *Phys Rev Lett* 97:187401. <https://doi.org/10.1103/PhysRevLett.97.187401>
- [62] Ferrari AC (2007) Raman spectroscopy of graphene and graphite: Disorder, electron-phonon coupling, doping and nonadiabatic effects. *Solid State Commun* 143:47–57. <http://doi.org/10.1016/j.ssc.2007.03.052>
- [63] Nemanich RJ, Solin SA (1979) First- and second-order Raman scattering from finite-size crystals of graphite. *Phys Rev B* 20:392. <https://doi.org/10.1103/PhysRevB.20.392>
- [64] Vidano RP, Fischbach DB, Willis LJ, Locher TM (1981) Observation of Raman band shifting with excitation wavelength for carbons and graphites. *Solid State Commun* 39:341–344. [https://doi.org/10.1016/0038-1098\(81\)90686-4](https://doi.org/10.1016/0038-1098(81)90686-4)
- [65] Lespade P, Marchand A, Couzi M, Cruege F (1984) Caractérisation de matériaux carbonés par microspectrométrie Raman. *Carbon N Y* 22:375–385. [https://doi.org/10.1016/0008-6223\(84\)90009-5](https://doi.org/10.1016/0008-6223(84)90009-5)
- [66] Vázquez-Santos MB, Geissler E, László K et al (2012) Comparative XRD, Raman, and TEM study on graphitization of PBO-derived carbon fibers. *J Phys Chem C* 116:257–268. <https://doi.org/10.1021/jp2084499>
- [67] Yin J, Slizovskiy S, Cao Y et al (2019) Dimensional reduction, quantum Hall effect and layer parity in graphite films. *Nat Phys* 15:437–442. <https://doi.org/10.1038/s41567-019-0427-6>
- [68] Cong C, Yu T, Sato K et al (2011) Raman characterization of ABA- and ABC-stacked trilayer graphene. *ACS Nano* 5:8760–8768. <https://doi.org/10.1021/nn203472f>
- [69] Jhang SH, Craciun MF, Schmidmeier S et al (2011) Stacking-order dependent transport properties of trilayer graphene. *Phys Rev B - Condens Matter Mater Phys* 84:161408(R). <https://doi.org/10.1103/PhysRevB.84.161408>
- [70] Mak KF, Shan J, Heinz TF (2010) Electronic structure of few-layer graphene: Experimental demonstration of strong dependence on stacking sequence. *Phys Rev Lett* 104:176404. <https://doi.org/10.1103/PhysRevLett.104.176404>
- [71] Cancado L, Takai K, Enoki T (2006) General equation for the determination of the crystallite size L_a of nanographite by Raman spectroscopy. *Appl Phys Lett* 88:163106. <https://doi.org/10.1063/1.2196057>
- [72] Qiu T, Yang JG, Bai XJ, Wang YL (2019) The preparation of synthetic graphite materials with hierarchical pores from lignite by one-step impregnation and their characterization as dye absorbents. *RSC Adv* 9:12737–12746. <https://doi.org/10.1039/c9ra00343f>
- [73] Xie X, Zhou Y, Bi H et al (2013) Large-range control of the microstructures and properties of three-dimensional porous graphene. *Sci Rep* 3:2117. <https://doi.org/10.1038/srep02117>
- [74] Kuang J, Liu L, Gao Y et al (2013) A hierarchically structured graphene foam and its potential as a large-scale strain-gauge sensor. *Nanoscale* 5:12171–12177. <https://doi.org/10.1039/c3nr03379a>
- [75] Kuila T, Mishra AK, Khanra P et al (2013) Recent advances in the efficient reduction of graphene oxide and its application as energy storage electrode materials. *Nanoscale* 5:52–71. <https://doi.org/10.1039/c2nr32703a>
- [76] Gupta G, Slanac DA, Kumar P et al (2010) Highly stable Pt/ordered graphitic mesoporous carbon electrocatalysts for oxygen reduction. *J Phys Chem C* 114:10796–10805. <https://doi.org/10.1021/jp907015j>
- [77] Forouzandeh F, Li X, Banham DW et al (2018) Understanding the corrosion resistance of meso- and micro-porous carbons for application in PEM fuel cells. *J Electrochem Soc* 165:F3230–F3240. <https://doi.org/10.1149/2.0261806jes>
- [78] Miller EM, Zhao Y, Mercado CC et al (2014) Substrate-controlled band positions in $\text{CH}_3\text{NH}_3\text{PbI}_3$ perovskite films. *Phys Chem Chem Phys* 16:22122–22130. <https://doi.org/10.1039/c4cp03533j>
- [79] Endres J, Egger DA, Kulbak M et al (2016) Valence and conduction band densities of states of metal halide perovskites: a combined experimental-theoretical study. *J Phys Chem Lett* 7:2722–2729. <https://doi.org/10.1021/acs.jpcclett.6b00946>
- [80] Tan HL, Abdi FF, Ng YH (2019) Heterogeneous photocatalysts: an overview of classic and modern approaches for optical, electronic, and charge dynamics evaluation. *Chem Soc Rev* 48:1255–1271. <https://doi.org/10.1039/c8cs00882e>
- [81] Nicholson RS (1965) Theory and Application of Cyclic Voltammetry for the Measurement of Electrode Reaction Kinetics. *Anal Chem* 37:1351–1355. <https://doi.org/10.1021/ac60230a016>
- [82] Ambrosi A, Chua CK, Bonanni A, Pumera M (2012) Lithium aluminum hydride as reducing agent for chemically reduced graphene oxides. *Chem Mater* 24:2292–2298. <https://doi.org/10.1021/cm300382b>
- [83] Sengupta R, Bhattacharya M, Bandyopadhyay S, Bhowmick AK (2011) A review on the mechanical and electrical properties of graphite and modified graphite reinforced polymer composites. *Prog Polym Sci* 36:638–670. <https://doi.org/10.1016/j.progpolymsci.2010.11.003>
- [84] Tao L, Qiao M, Jin R et al (2019) Bridging the surface charge and catalytic activity of a defective carbon electrocatalyst. *Angew Chemie Int Ed* 58:1019–1024. <https://doi.org/10.1002/anie.201810207>

- [85] Yan X, Tian L, Murowchick J, Chen X (2016) Partially amorphized MnMoO_4 for highly efficient energy storage and the hydrogen evolution reaction. *J Mater Chem A* 4:3683–3688. <https://doi.org/10.1039/c6ta00744a>
- [86] Maass S, Finsterwalder F, Frank G et al (2008) Carbon support oxidation in PEM fuel cell cathodes. *J Power Sources* 176:444–451. <https://doi.org/10.1016/j.jpowsour.2007.08.053>
- [87] Randviir EP, Banks CE (2013) Electrochemical impedance spectroscopy: An overview of bioanalytical applications. *Anal Methods* 5:1098–1115. <https://doi.org/10.1039/c3ay26476a>
- [88] Song Y, Hu H, Feng M, Zhan H (2015) Carbon nanotubes with tailored density of electronic states for electrochemical applications. *ACS Appl Mater Interfaces* 7:25793–25803. <https://doi.org/10.1021/acsami.5b07700>
- [89] Ambrosi A, Bonanni A, Sofer Z et al (2011) Electrochemistry at chemically modified graphenes. *Chem - A Eur J* 17:10763–10770. <https://doi.org/10.1002/chem.201101117>
- [90] Joachim C, Gimzewski JK, Aviram A (2000) Electronics using hybrid-molecular and mono-molecular devices. *Nature* 408:541–548. <https://doi.org/10.1038/35046000>
- [91] Avasarala B, Moore R, Haldar P (2010) Surface oxidation of carbon supports due to potential cycling under PEM fuel cell conditions. *Electrochim Acta* 55:4765–4771. <https://doi.org/10.1016/j.electacta.2010.03.056>

Publisher's Note Springer Nature remains neutral with regard to jurisdictional claims in published maps and institutional affiliations.